Inorg. Chem. **2003**, *42*, 446–456

Computational Study of the Non-Heme Iron Active Site in Superoxide Reductase and Its Reaction with Superoxide

Radu Silaghi-Dumitrescu,[†‡] Ioan Silaghi-Dumitrescu,[‡] Eric D. Coulter,[†] and Donald M. Kurtz, Jr.*[,†]

Department of Chemistry and Center for Metalloenzyme Studies, University of Georgia, Athens, Georgia 30602, and Department of Chemistry, "Babeş-Bolyai" University, Cluj-Napoca RO-3400, Romania

Received April 29, 2002

The ferrous square-pyramidal [Fe(NHis)$_4$(SCys)] site of superoxide reductases (SORs) has been shown to reduce superoxide at a nearly diffusion-controlled rate. The final products of the reaction are hydrogen peroxide and the ferric hexacoordinated SOR site, with a carboxylate group from a conserved glutamate serving as the sixth ligand trans to the cysteine sulfur. A transient intermediate absorbing at ~600 nm in the reaction of the ferrous pentacoordinated site with superoxide has been proposed to be a ferric-(hydro)peroxo complex (Coulter, E.; Emerson, J.; Kurtz, D. M., Jr.; Cabelli, D. *J. Am. Chem. Soc.* **2000**, *122*, 11555–11556.). In the present study, DFT and ZINDO/S-CI results are shown to support the description of the 600-nm intermediate as an end-on, low-spin ferric-peroxo or -hydroperoxo complex. Side-on peroxo coordination was found to be significantly less stable than end-on because of constraints on the imidazole ligand ring orientations imposed mostly by the protein. The modeled ferric-hydroperoxo complex had a decidedly nonplanar Cys$C\beta$–S–Fe–O–O geometry that appears to be imposed by the same constraints. A single prominent visible absorption of the (hydro)peroxo model is shown to be due mainly to a CysS → Fe(III) π charge transfer (CT) transition with a minor portion of His → Fe(III) π CT character and very little peroxo → Fe(III) CT character. On the basis of calculations of models with various mono- and diprotonated peroxo ligands, protonation of the iron-bound peroxo oxygen is a key step in the decay of the ferric-(hydro)peroxo complex favoring release of hydrogen peroxide over cleavage of the O–O bond, as occurs in the heme structural analogue, cytochrome P450.

Introduction

Superoxide reductase (SOR), an enzyme found in several air-sensitive bacteria and archaea, catalyzes the one-electron reduction of superoxide to hydrogen peroxide at a unique square-pyramidal ferrous [Fe(NHis)$_4$(SCys)] site.[1−4] The "resting" ferric form of this site is pseudo-octahedral, with a carboxylate from a conserved glutamate occupying the sixth coordination position, trans to the cysteine ligand.[1] The structures of the resting ferrous and ferric SOR sites (depicted in Scheme 1) have been verified by X-ray crystallography.[1,2] The resting ferric SOR site exhibits ligand-to-metal charge transfer (LMCT) absorptions at ~340 nm and ~650 nm (ϵ_{650} ~ 2000 cm^{-1}).[5−7] Pulse radiolysis studies of *D. vulgaris* SOR reported that the ferrous SOR site reacted with superoxide in a nearly diffusion-controlled, second-order process (~10^9 M^{-1} s^{-1}) to give an intermediate which exhibited an intense absorption at ~600 nm (ϵ_{600} ~ 3500 M^{-1} cm^{-1}).[8,9] This intermediate then decayed to the "resting" ferric SOR form in a first-order process (~50 s^{-1}). As shown in Scheme 1,

* To whom correspondence should be addressed at the Department of Chemistry. E-mail: kurtz@chem.uga.edu. Fax: 706-542-9454.
† University of Georgia.
‡ "Babeş-Bolyai" University.

(1) Yeh, A.; Hu, Y.; Jenney, F. J.; Adams, M.; Rees, D. *Biochemistry* **2000**, *39*, 2499−2508.
(2) Coelho, A.; Matias, P.; Fulop, V.; Thompson, A.; Gonzalez, A.; Carrondo, M. *JBIC, J. Biol. Inorg. Chem.* **1997**, *2*, 680−689.
(3) Jenney, F. J.; Verhagen, M.; Cui, X.; Adams, M. *Science* **1999**, *286*, 306−308.
(4) Coulter, E.; Kurtz, D. M., Jr. *Arch. Biochem. Biophys.* **2001**, *394*, 76−86.
(5) Tavares, P.; Ravi, N.; Moura, J.; LeGall, J.; Huang, Y.; Crouse, B.; Johnson, M. K.; Huynh, B.; Moura, I. *J. Biol. Chem.* **1994**, *269*, 10504−10510.
(6) Clay, M. D.; Jenney, F. E. J.; Noh, H. J.; Hagedoorn, P. L.; Adams, M. W. W.; Johnson, M. K. *Biochemistry* **2002**, *41*, 9833−9841.
(7) Clay, M. D.; Jenney, F. J.; Hagedoorn, P.; George, G.; Adams, M.; Johnson, M. K. *J. Am. Chem. Soc.* **2002**, *124*, 788−805.
(8) Coulter, E.; Emerson, J.; Kurtz, D. M., Jr.; Cabelli, D. *J. Am. Chem. Soc.* **2000**, *122*, 11555−11556.
(9) Emerson, J.; Coulter, E.; Cabelli, D.; Phillips, R.; Kurtz, D. M., Jr. *Biochemistry* **2002**, *41*, 4348−4357.

10.1021/ic025684l CCC: $25.00 © 2003 American Chemical Society
Published on Web 12/20/2002

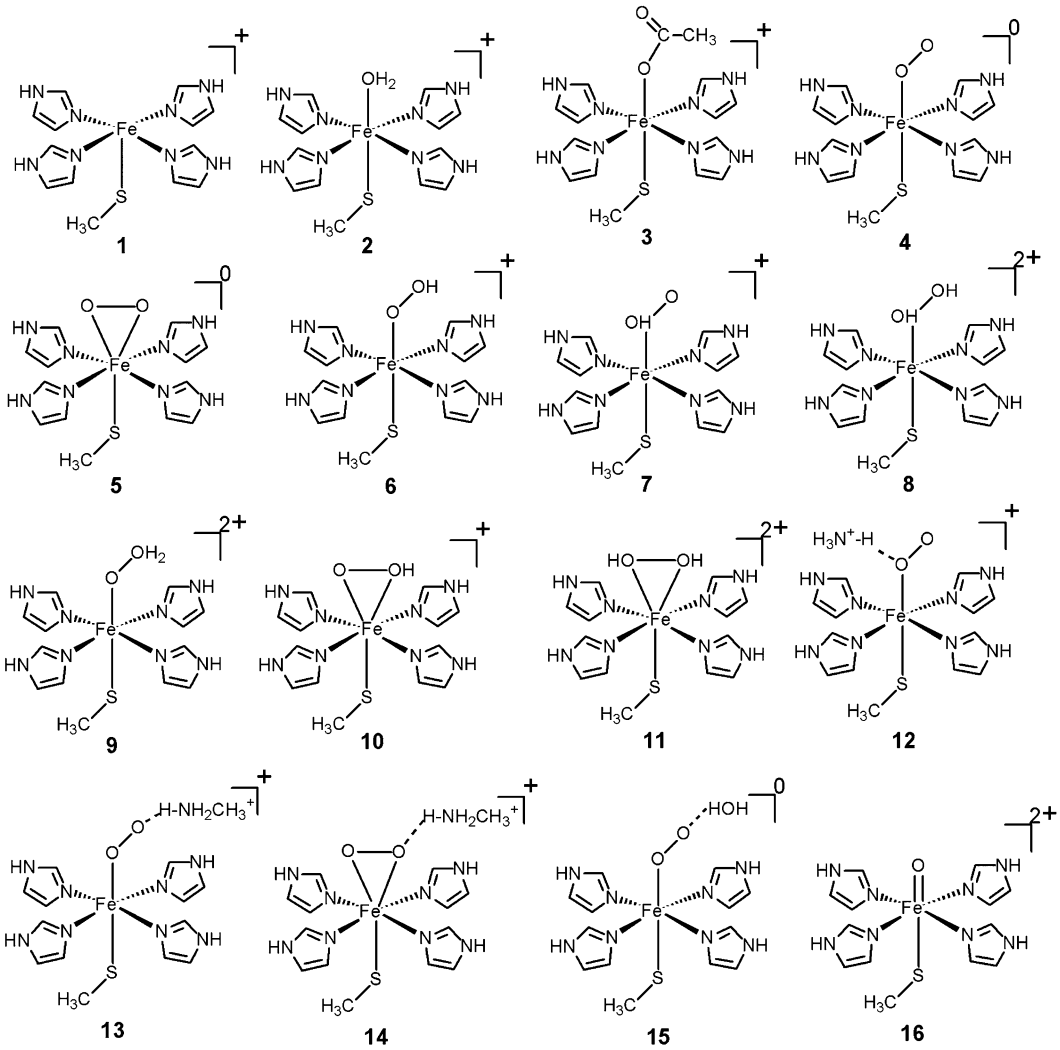

Figure 1. The sixteen models of the SOR active site that were investigated in this study. See Scheme 2 for atom labeling and imidazole numbering.

Scheme 1

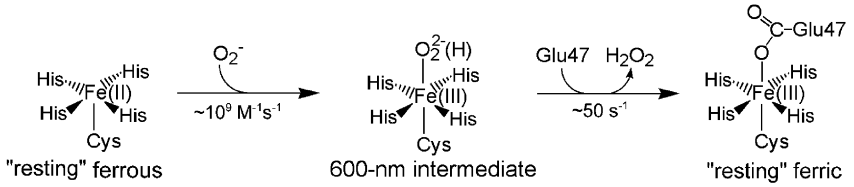

the 600-nm intermediate was formulated to be a ferric-(hydro)peroxo species. Subsequent pulse radiolysis studies on some other SORs have described either one[10] or two[11,12] consecutive intermediates, variously formulated as ferrous-superoxo, ferric-peroxo, or ferric-hydroperoxo. However, the exact nature of the 600-nm intermediate or of the subsequently reported intermediates has not been established.

Density functional theory (DFT) and Zerner's INDO/S semiempirical method with configuration interaction (ZINDO/S-CI) are being increasingly applied to characterization of geometries and electronic structures of transition metal enzyme active sites and to their reaction mechanisms.[13−15] In the present study, DFT geometry optimizations were performed for models of the well-characterized ferrous pentacoordinated and ferric glutamate-bound forms of the SOR site (**1**, **3** in Figure 1), as well as for various putative ferric-peroxo and ferric-hydroperoxo SOR complexes (**4**−**15** in Figure 1). Electronic absorption spectra were computed using ZINDO/S-CI, for a low-spin ferric-hydroperoxo model of the SOR active site, which is suggested by the DFT results to be the best candidate of those examined for the 600-nm

(10) Abreu, I.; Saraiva, L.; Soares, C.; Teixeira, M.; Cabelli, D. *J. Biol. Chem.* **2001**, *276*, 38995−39001.
(11) Lombard, M.; Houee-Levin, C.; Touati, D.; Fontecave, M.; Niviere, V. *Biochemistry* **2001**, *40*, 5032−5050.
(12) Niviere, V.; Lombard, M.; Fontecave, M.; Houee-Levin, C. *FEBS Lett.* **2001**, *497*, 171−173.
(13) Loew, G. H.; Harris, D. L. *Chem. Rev.* **2000**, *100*, 407−419.
(14) Siegbahn, P. E. M.; Blomberg, M. R. A. *Annu. Rev. Phys. Chem.* **1999**, *50*, 221−49.
(15) Siegbahn, P. E. M.; Blomberg, M. R. A. *Chem. Rev.* **2000**, *100*, 421−437.

Table 1. Summary of Relevant Interatomic Distances (Å) and Dihedral Angles (deg) for the [Fe(NHis)$_4$(SCys)] Site in SORs from the Available Crystal Structures and EXAFS Data

source[a]	Fe−NHis$_{av}$	Fe−S	Fe−O[b]	Fe−NH$_3$[c]	θ_1[d]	θ_2[e]	θ_3[f]
1DFX	2.1	2.3	10.8	7.5	17	6	64
1DO6	2.1	2.3	7.8	3.5	18	12	73
1DO6	2.1	2.4	2.0	11.7	18	13	75
1DQI	2.1	2.7	8.3 (2.6)	5.9	10	9	75
1DQI	2.1	2.5	2.1	12	10	16	78
1DQI	2.1	2.7	10.7 (2.6)	6.6	10	17	75
1DQI	2.2	2.5	2.1	12	11	14	76
1DQK	2.4	2.7	8.6	8.9	−12	8	58
1DQK	2.1	2.4	7.1	7.1	6	16	83
1DQK	2.1	2.6	10.7 (5.7)	7.6	−6	4	72
1DQK	2.1	2.4	7.1 (4.6)	6.8	7	7	85
EXAFS, Fe^{3+}	2.1−2.2	2.4	2.1				
EXAFS, Fe^{2+}	2.1−2.2	2.4					

[a] Sources are listed either as Protein Databank identification codes for crystal structures (1DFX from *D. desulfuricans* SOR, all others from *P. furiosus* SOR), or as EXAFS-determined distances. [b] Distance between iron and the carboxylate Oϵ2 of Glu47, or, in parentheses, Fe−OH$_2$ distance when a proximal water molecule is present. [c] Distance from iron to the ϵ-amino nitrogen of Lys48. [d] Cys116Cβ−S−Fe−NϵHis49 dihedral angle. [e] Cys116S−Fe−Nϵ−CδHis75 dihedral angle. [f] His69Cϵ−Nϵ−Nδ−CγHis119 dihedral angle. Atom labels are shown in Scheme 2.

intermediate. The reactivity of the seemingly similar heme-thiolate active site in cytochrome P450 is compared with that of the SORs.

Methods

Models Used and Choice of Initial Geometries. The models employed in this study are shown in Figure 1. $S = 0$, 1, and 2 spin states for formally Fe(II) and $S = {}^5/_2$, ${}^3/_2$, and ${}^1/_2$ for formally Fe(III) complexes were examined. To relate our results to the protein, the *D. vulgaris* SOR amino acid sequence numbering (Genbank accession number P20418) is used throughout.[16]

All models were constructed within the Builder module of the *Spartan*[17] package. All of the models contained either a ferric or ferrous iron coordinated axially by a methyl thiolate (SCH_3^-) and equatorially by four neutral (protonated) imidazole ligands (cf. Figure 1). This basic structure (**1** in Figure 1) was used to model the "resting" ferrous SOR site. The starting geometries of all models were varied in order to avoid local energy minima upon geometry optimization. A six-coordinate ferrous model of the SOR site with water as the sixth (axial) ligand (**2** in Figure 1) was also examined, because the *P. furiosus* SOR crystal structure (PDB ID 1DQI) shows two long (2.6 Å) Fe−OH$_2$ contacts (presumed to be in ferrous sites, vide infra). The glutamate ligand in the resting ferric state was modeled as acetate (**3** in Figure 1). Pentacoordinated models were generated using the corresponding atomic coordinates from the *D. desulfuricans* SOR crystal structure (PDB entry 1DFX, cf. Table 1), while hexacoordinated models were generated using the corresponding atomic coordinates from the *P. furiosus* oxidized SOR crystal structure (cf. Table 1, PDB entries 1DO6 and 1DQI). Pentacoordinated models constructed from the *P. furiosus* SOR crystal structure (PDB entries 1DQK, 1DQI, and 1DO6) yielded upon geometry optimization results identical to those obtained using

Scheme 2

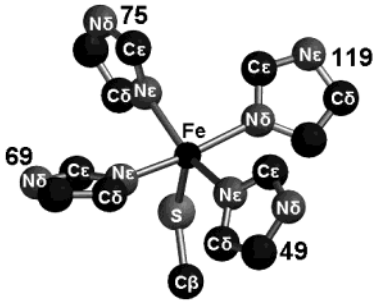

the model constructed from the *D. desulfuricans* (1DFX) SOR crystal structure. Models **4**−**11** were constructed by substituting a dioxygen ligand in the position occupied by acetate in model **3**. The charge on the dioxygen complexes was assigned so as to describe the putative product of a reaction between the ferrous pentacoordinated model and a superoxide moiety, which would subsequently undergo protonation, as outlined in Scheme 1. Models **12**−**14** (Figure 1) were constructed from models **6** and **5**, respectively, by placing a methylammonium ion within NH···O(peroxo) hydrogen bonding distance of each dioxygen atom, to model a conserved proximal lysine residue. Model **15** was constructed from model **4** by placing a water molecule within hydrogen bonding distance of the non-iron-coordinated dioxygen atom.

The imidazole numbering[16] and atom labeling schemes are shown in Scheme 2. Results are presented using the following conventions: the *z*-axis is defined by the S−Fe bond, and the *x*- and *y*-axes lie (approximately) along the N−Fe−N bonds involving imidazoles 49/75 and 69/119, respectively. The imidazole ring orientations were constrained in all the models to accurately reflect those in the SOR crystal structures (cf. Scheme 2 and Table 1). These constraints placed the Cϵs of imidazoles 119, 75, and 49 on the side of the *xy*-plane opposite the methyl thiolate, and Cβ of imidazole 69 on the same side of the *xy*-plane as the methyl thiolate. In models **4**−**15**, the O−O bond of the dioxygen moiety was sterically constrained by the orientations of imidazole rings 49 and 75 to lie approximately along the *y*-axis. A further constraint in SORs is that the hydrophobic side chain of a conserved Pro68 lying above His69 and a protein backbone loop including Lys48 would sterically force an incoming superoxide molecule to approach the open coordination position of the ferrous SOR site approximately along the *y*-axis from above imidazole 119. The starting end-on dioxygen-coordinated models used in this study were, therefore, constructed with the non-iron-bound dioxygen atom pointing toward imidazole 119 rather than imidazole 69.

Computational Methods. Geometries for models **1**−**16** were optimized at the DFT level in the *Spartan* package at the University of Georgia Scientific Visualization and Molecular Graphics facility. The BP86 functional, which uses the gradient-corrected exchange functional proposed by Becke (1988), the correlation functional by Perdew (1986), and the DN** numerical basis set (comparable in size to 6-31G**) were used as implemented in *Spartan*.[17] For the SCF calculations, a fine grid was used, and the convergence criteria were set to 10^{-6} (for the root-mean square of electron density) and 10^{-8} (energy), respectively. For geometry optimization, convergence criteria were set to 0.001 au (maximum gradient criterion) and 0.0003 (maximum displacement criterion). Charges and spin densities were derived from Mulliken population analyses after DFT geometry optimization. ZINDO/S-CI calculations were performed

(16) To adjust the sequence numbering in the crystal structures to the *D. vulgaris* SOR numbering used here, 1 should be added to the residue numbers in the *D. desulfuricans* SOR structure and 33 (for Glu14, Lys15, His16), 28 (for His41 and His47), or 5 (for His114) should be added to the residue numbers in the *P. furiosus* SOR structures.

(17) (a) *Spartan 5.0*; Wavefunction, Inc.: Irvine, CA. (b) Becke, A. D. *Phys. Rev.* **1988**, *A38*, 3089. (c) Perdew, J. P. *Phys. Rev.* **1986**, *B33*, 8822.

on the DFT-optimized structures in the *Hyperchem*[18] package at the "Babeş-Bolyai" University in Cluj-Napoca, Romania. Windows were manually defined for the configuration interaction on the basis of energy as well as symmetry considerations so as to include the valence orbitals on iron and its ligands, while not artificially biasing toward any one of the imidazole ligands.

Results

Table 1 lists relevant structural parameters from the available SOR crystal structures and EXAFS measurements, Figure 1 illustrates the models examined in this study, and Scheme 2 depicts the atom labeling and imidazole numbering scheme.[16] The oxidation state of iron in some of the SOR crystal structures is ambiguous because of the ease of reduction of the ferric site.[1,5,7,8] On the basis of spectroscopic and mutational results,[7] we assume that those structures having a coordinating glutamate (Fe−O distances of 2.0−2.1 Å in Table 1) are ferric, and that the pentacoordinated structures are ferrous. The reported Fe−S bond lengths in the available crystal structures vary from 2.3 to 2.7 Å. The higher end of this range may be unrealistic. At least one 2.6-Å and one 2.7-Å Fe−SCys distance are likely to be less accurate than the others because of the low occupancy of the iron sites,[1] and the other two 2.7-Å Fe−S distances are in subunits whose iron sites exhibited higher disorder. An Fe−SCys distance of 2.4 Å was reported for EXAFS[7] of both ferric and ferrous *P. furiosus* SOR. The Fe−NHis distances vary in the crystal structures between 2.0 and 2.4 Å, with four outliers at 1.9, 2.7, 2.7, and 3.05 Å occurring in the subunits with lower iron occupancies. Because we could discern no distinct pattern in the variation of Fe−NHis distances from the available structural data, only averages are listed. This statement includes His119, which in the SORs is Nδ-ligated to iron, whereas the other three His residues are Nϵ-ligated. Nonbonding distances listed in Table 1 include Fe−O of solvent molecules observed near the open coordination sites in four of the *P. furiosus* SOR subunits, and Fe−N distances of 3.5−11.7 Å between iron and the ϵ-amino nitrogen of conserved Lys48.

The sequentially adjacent conserved residues Glu47 and Lys48 are located on a solvent-exposed and highly mobile loop of the SOR polypeptide. In the *P. furiosus* SOR crystal structures, when the Glu47 carboxylate is not coordinated to iron, it appears to be hydrogen-bonded to Nδ of the iron-ligated His49 (the carboxylato-O···NδHis distance varies from 3 to 4.3 Å). We have treated all nonligating imidazole nitrogens in the models as protonated, that is, as neutral imidazole ligands.[19]

At least one peptide NH···SCys ligand hydrogen bond exists at the SOR active site. Such hydrogen bonding to thiolate ligands is ubiquitous in metalloproteins; that is, this feature is not unique to SORs. We have not included this NH···S interaction in our models, because neither DFT nor ZINDO is likely to accurately model these interactions.

Dihedral Angle Constraints. The only geometrical constraints applied to the models were the dihedral angles $\theta_1-\theta_3$, listed in Table 1, defining the orientations of the imidazole rings. These angles are restricted to relatively small ranges in SORs but were found to change significantly upon geometry optimization of our models. In test calculations, geometry optimization led to migration of the methyl group of the coordinated methylthiolate, such that the $H_3C-S-Fe-N-His49$ dihedral angle, θ_1, increased from 17° to ∼45°. Geometry optimization also resulted in rotation of three of the imidazole rings from their positions shown in Scheme 2, such that the ring planes of imidazoles 69 and 119 tended to become quasiparallel to the *z*-axis (i.e., the Fe−S bond axis), whereas that of imidazole 75 rotated ∼45° away from its quasiparallel orientation to the *z*-axis. The imidazole 49 ring plane was apparently restricted from reorienting by steric interactions with the thiolate methyl group. In SORs, steric restrictions imposed by the protein matrix,[20] and attachments to the protein backbone, particularly the Cys116-Asn117-Leu118-His119 tetrapeptide "chelation" of iron, would prevent rotation of the three corresponding His rings and Cys side chain to the DFT-optimized orientations. Therefore, geometries for all models were also DFT-optimized with the $\theta_1-\theta_3$ dihedral angles constrained to the values seen in the SOR crystal structure, 1DFX (cf. Table 1). Depending on the model, the differences in bond lengths between the optimized geometries obtained with versus without the dihedral angle constraints varied from 0 to 0.05 Å.[21] These constraints did not affect the relative stabilities of the spin states for any of the models examined. Therefore, only results obtained with dihedrals $\theta_1-\theta_3$ constrained to their 1DFX values are reported.

Reaction of SOR with Superoxide. Scheme 3 presents three possible pathways of reaction of the "resting" ferrous SOR site with superoxide leading to the resting ferric state, some of which have been suggested previously.[3,7−12,22] All of the modeling results discussed in the following paragraphs address structural, electronic, and mechanistic questions posed by the pathways diagrammed in Scheme 3.

The Ferrous Pentacoordinated SOR Model (1). The ferrous SOR site is known to be high-spin ($S = 2$).[5,7] Geometry optimizations showed the high-spin state of the ferrous pentacoordinated model **1** (cf. Figure 1) to be slightly more stable than the $S = 1$ and $S = 0$ states. Calculated energies and iron−ligand distances are listed in Table 2, and atomic partial charges are listed in Table 3. The overall square-pyramidal coordination geometry of the iron observed in the crystal structures was not altered by the DFT geometry

(18) *HyperChem Molecular Modelling System*, Release 4.5 SGI, Hypercube; Hypercube, Inc. *Hyperchem Molecular Modelling System*, Release 5.01 for Windows; Hypercube, Inc.

(19) His49 Nδ in the *D. desulfuricans* SOR crystal structure appears to be involved in an unusual hydrogen bond with a main-chain peptide NH, implying a deprotonated imidazole ligand. However, this interaction is not present in any of the *P. furiosus* SOR X-ray structures.

(20) These steric constraints are imposed by interactions with conserved Trp122, Pro70, Leu118, and Ile77, as well as by interactions between the His119 Cβ and His49 heterocycle, and between each of the adjacent histidine ring planes.

(21) Calculated values of the S−Fe−NeHis49 and Cys116Cβ−S−Fe angles were independent of the geometrical constraints imposed on the dihedral angles, and similar to the values observed in the SOR crystal structures.

(22) Adams, M. W. W.; Jenney, F. E.; Clay, M. D.; Johnson, M. K. *JBIC, J. Biol. Inorg. Chem.* **2002**, *7*, 647−652.

Scheme 3

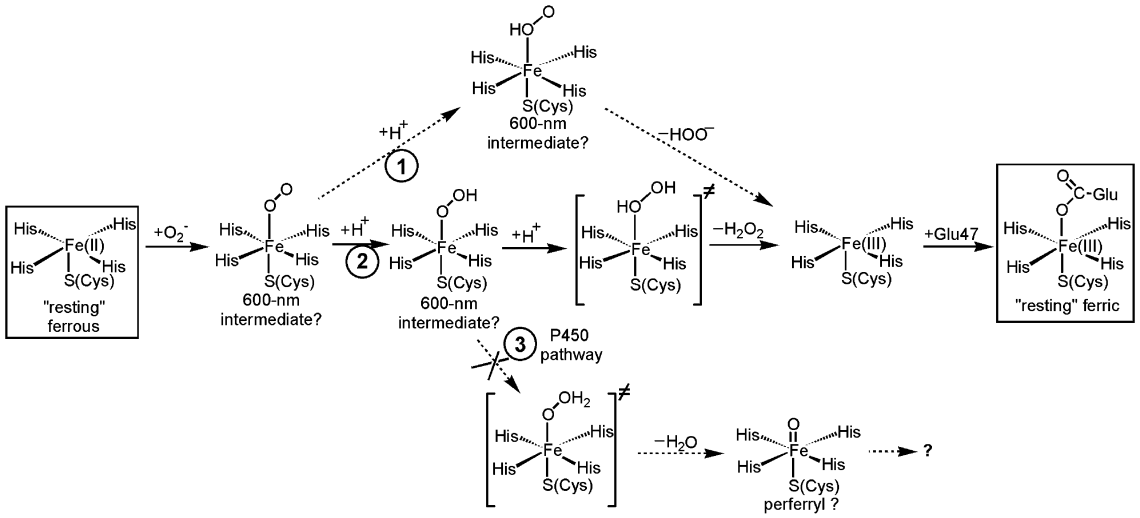

Table 2. Energies (kJ/mol), Distances (Å), and Angles (deg) Obtained after DFT Geometry Optimization of Selected SOR Active Site Models

model[a]	energy	Fe−S	Fe−N	Fe−O	O−O	O_2−H	Fe−O−O angle	N119−Fe−O−O dihedral[f]
1, $S = 0$	−6 845 591	2.26	1.98					
1, $S = 1$	−6 845 597	2.25	2.24					
1, $S = 2$	−6 845 603	2.25	2.20					
2, $S = 2$	−7 046 383	2.29	2.21	2.80				
3, $S = 1/2$	−7 445 762	2.19	2.03	2.03			148[b]	
3, $S = 3/2$	−7 445 777	2.21	2.18	2.02			176[b]	
3, $S = 5/2$	−7 445 800	2.34	2.20	2.01			161[b]	
4, $S = 1/2$	−7 241 028	2.43	2.01	1.90	1.37		123	−27
4, $S = 3/2$	−7 240 966	2.35	2.17	1.88	1.36		128	−17
4, $S = 5/2$	−7 240 962	2.45	2.28	1.89	1.37		156	−6
5, $S = 5/2$	−7 240 982	2.48	2.34[e]	2.01/2.04	1.42		71/68[d]	−1
6, $S = 1/2$	−7 242 236	2.28	2.02	1.87	1.51	0.98	119	45
6, $S = 3/2$	−7 242 188	2.31	2.20	1.84	1.51	0.98	118	−2
6, $S = 5/2$	−7 242 180	2.36	2.22	1.99	1.47	0.98	120	−15
7, $S = 1/2$	−7 242 133	2.23	2.01	2.06	1.44	0.98	120	27
7, $S = 3/2$	−7 242 084	2.25	2.21	2.00	1.44	0.99	127	37
7, $S = 5/2$	−7 242 090	2.29	2.25	2.18	1.42	0.99	129	4
12, $S = 1/2$	−7 493 952	2.23	2.01	2.03	1.42	1.02	128	−27
12, $S = 5/2$	−7 493 910	2.29	2.21	2.14	1.44	1.05	130	−32
13, $S = 1/2$[g]	−7 494 022	2.30	2.03	1.90	1.49	1.01	120	−34
13, $S = 5/2$[g]	−7 493 959	2.37	2.22	2.00	1.45	1.02	120	−35
15, $S = 1/2$	−7 441 853	2.42	2.03	1.90	1.40	1.71	123	−38
16, $S = 1/2$	−7 042 298	2.30	2.03	1.66				
16, $S = 3/2$	−7 242 084	2.42	2.02	1.68				

[a] Models listed according to their numbers in Figure 1. [b] Fe−O−C angle. [c] Only three histidine ligands (see text). [d] Both Fe−O−O angles are listed. [e] With two Fe−N bonds at 2.43 (imidazole 119) and 2.40 (imidazole 69), respectively. [f] Corresponds to the angle, β, in Figure 5. The values of the respective Cβ−S···O−O dihedral angles, α, in Figure 5, can be obtained by adding 106° to the values listed in this table. [g] Same as **14**.

optimization. In high-spin ($S = 2$) model **1**, the iron atom was found to be pulled toward the sulfur ligand, ∼0.5 Å out of the average plane defined by the four nitrogen ligands. Similar displacements are seen in the SOR crystal structures (∼0.3 Å in the pentacoordinated sites, ∼0.2 Å in the hexacoordinated sites), and in all hexacoordinated models examined in the present study (∼0.1 Å in low-spin models, ∼0.2 Å in high-spin models). The optimized Fe−S (2.26 Å) and Fe−N (2.20 Å) bond distances in high-spin ($S = 2$) model **1** are in reasonable agreement with the corresponding distances in the 1DFX crystal structure (2.3 and 2.1 Å, respectively), and with those determined by EXAFS of *P. furiosus* SOR.[7] A space-filling depiction of the DFT-optimized high-spin ($S = 2$) model **1** is shown in Figure 2.

The frontier orbitals of model **1** are potential candidates for interacting with incoming ligands, such as superoxide. As shown in Figure 3, all calculated HOMOs in high-spin model **1** are antibonding and show strong iron d orbital character. The calculated LUMOs, on the other hand, have no significant iron character and are, therefore, unlikely to be involved in reactions of the iron with incoming ligands.

Water as a Ligand to the Ferrous SOR Model (2). The optimized geometry for the $S = 2$ ferrous SOR model with a sixth axial aqua ligand (model **2** in Figure 1) yielded a reasonable Fe−S bond distance of 2.29 Å but an Fe−OH_2 distance at 2.8 Å that is too long for a bonding interaction (using various Fe−OH_2 distances, between 1.6 and 2.8 Å, as starting points for geometry optimization). Upon geometry optimization, the water protons were tilted toward the imidazoles, down and away from the *z*-axis.

The Ferric Acetate Complex (3). The resting ferric SOR site (cf. Scheme 3), which is known to be high-spin ($S =$

Table 3. Relevant Partial Atomic Charges for Selected Models of the SOR Site

model[a]	Fe	S	O1[b]	O2[b]
1, $S = 0$	0.40	−0.23		
1, $S = 0$	0.50	−0.28		
1, $S = 2$	0.54	−0.22		
2, $S = 2$	0.47	−0.27		
3, $S = {}^1/_2$	0.53	−0.10	−0.51	−0.53
3, $S = {}^3/_2$	0.71	−0.11	−0.52	−0.53
3, $S = {}^5/_2$	0.88	−0.22	−0.52	−0.50
4, $S = {}^1/_2$	0.50	−0.40	−0.28	−0.38
4, $S = {}^3/_2$	0.62	−0.35	−0.29	−0.37
4, $S = {}^5/_2$	0.78	−0.44	−0.33	−0.40
5, $S = {}^5/_2$	0.83	−0.43	−0.37	−0.39
6, $S = {}^1/_2$	0.53	−0.21	−0.38	−0.31
6, $S = {}^3/_2$	0.79	−0.29	−0.38	−0.30
6, $S = {}^5/_2$	0.86	−0.26	−0.42	−0.27
7, $S = {}^1/_2$	0.50	−0.14	−0.27	−0.44
7, $S = {}^3/_2$	0.66	−0.17	−0.25	−0.40
7, $S = {}^1/_2$	0.84	−0.24	−0.28	−0.40
12, $S = {}^1/_2$	0.49	−0.22	−0.32	−0.39
12, $S = {}^5/_2$	0.94	−0.29	−0.38	−0.48
13, $S = {}^1/_2$[c]	0.52	−0.16	−0.44	−0.33
13, $S = {}^5/_2$[c]	0.85	−0.29	−0.41	−0.33
15, $S = {}^1/_2$	0.50	−0.25	−0.28	−0.42
16, $S = {}^1/_2$	0.57	0.02	−0.32	
16, $S = {}^3/_2$	0.63	−0.04	−0.34	

[a] Models listed according to their numbers in Figure 1. [b] O1 and O2 are the iron-bound and nonbound oxygen atoms, respectively. [c] Same as **14**.

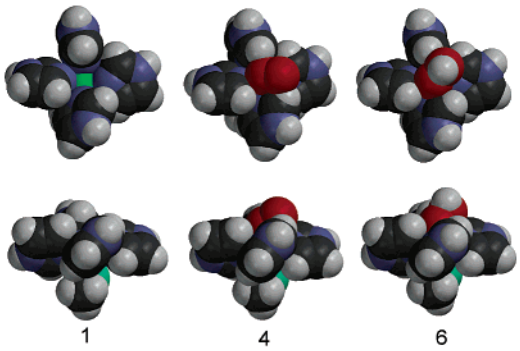

Figure 2. Space-filling depictions of the DFT-optimized $S = 2$ ferrous pentacoordinated (**1**) and $S = {}^1/2$ end-on, ferric-peroxo (**4**) and -hydroperoxo (**6**) models. Each model is shown in two viewing perspectives: parallel (top) and perpendicular (bottom) to the Fe−S axis. In the "parallel" view, SCH_3 is invisible behind Fe; in the "perpendicular" view, SCH_3 is pointing downward. In both viewing perspectives, imidazole 119 is to the right. Color coding: oxygen, red; iron, green; nitrogen, blue; carbon, dark gray; hydrogen, light gray; sulfur, cyan.

$^5/_2$),[5,7] was modeled as the ferric acetate complex, **3** (cf. Figure 1). Geometry optimizations showed high-spin model **3** to be more stable than the corresponding $S = {}^3/_2$ and $S = {}^1/_2$ states by 38 and 23 kJ/mol, respectively. Energies and iron−ligand distances for DFT-optimized model **3** are listed in Table 2, and partial atomic charges are listed in Table 3. The computed Fe−S distance for high-spin ($S = {}^5/_2$) model **3** was 2.34 Å, which is longer than that calculated for the ferrous high-spin pentacoordinated model **1**, but in reasonable agreement with the SOR crystal structures[1] and EXAFS[7] data, which show Fe−S bond distances of 2.5 Å (1DQI), 2.4 Å (1DO6), and 2.36 Å (EXAFS) for the Glu-ligated ferric hexacoordinated sites.

$[FeO_2]^+$ and $[FeO_2H]^{2+}$ Complexes. Geometries were optimized for $S = {}^5/_2$, $^3/_2$, and $^1/_2$ spin states of the [ferrous-superoxo ↔ ferric-peroxo] and the corresponding monoprotonated forms, considering end-on as well as side-on coordination of the dioxygen moiety, models **4**−**7**, **10**, **12**−**15** in Figure 1. Table 2 lists energies and geometrical parameters, and Table 3 lists partial atomic charges obtained for the DFT-optimized end-on $[FeO_2]^+$ and $[FeO_2H]^{2+}$ models. Upon geometry optimization, model **10** (side-on coordinated O−OH) became identical to **6** (end-on coordinated O−OH) for all spin states, while $S = {}^3/_2$ model **5** (side-on O−O) became identical to **4** (end-on O−O). Geometry optimization of low-spin model **5** resulted in displacement of one of the imidazole ligands (119) from the iron coordination sphere by one of the dioxygen atoms, and its parameters are, therefore, not included in Tables 2 and 3. High-spin ($S = {}^5/_2$) model **5** showed two very long (2.4-Å) Fe−N distances. These highly distorted structures for DFT-minimized models **5**, featuring side-on O−O coordination, are unlikely to be achievable at the highly constrained SOR site without severe disruption of the protein matrix. These distortions and rearrangements, thus, favor the end-on over the side-on O−O coordination at the SOR site. Furthermore, on the basis of the energies reported in Table 2, the most stable $[FeO_2]^+$ model is calculated to be low-spin, end-on **4**, while the most stable $[FeO_2H]^+$ model is calculated to be low-spin, end-on **6**. Thus, of the models examined, low-spin, end-on O−O coordinated models appear to be the two most likely candidates for the experimentally observed 600-nm intermediate. Space-filling depictions of the low-spin, end-on coordinated models **4** and **6** are shown in Figure 2.

The O−O bond lengths have been classified experimentally to fall in the range 1.24−1.31 Å for metal-superoxo complexes, and 1.35−1.5 Å for metal-peroxo complexes.[23] The computed O−O bond lengths in Table 2 are all ≥1.36 Å, consistent with ferric-peroxo character. In the end-on model **6**, the O−O bond lengths (1.51−1.47 Å) are clearly indicative of a ferric-hydroperoxo moiety. The calculated partial charges on iron for low-spin models **4** and **6** (cf. Table 3) are both ∼0.5, which, by comparison with those of the less ambiguous low-spin ferrous and ferric models **1** (0.40) and **3** (0.53), respectively, also indicate that ferric-(hydro)-peroxo is a more accurate description than ferrous-superoxo. Similar observations can be made with respect to iron partial charges in the less stable $S = {}^3/_2$ and $S = {}^5/_2$ states of models **4** and **6**, respectively. The substantial partial negative charges on the oxygen atoms in the O_2(H) ligand of models **4** and **6** (cf. Table 3) are also consistent with a peroxo formulation. We, therefore, hereafter refer to these models as ferric-peroxo and -hydroperoxo, respectively. The same observations with respect to partial atomic charges and ferric-peroxo character are valid for hydroperoxo models **7**, in which the coordinated rather than terminal oxygen is protonated. However, these models are calculated to be significantly less stable than their terminal oxygen protonated isomers, models **6**. This lower stability is consistent with the partial charge distribution in ferric-peroxo models **4** (cf. Table 3), where the terminal oxygen atom bears a more negative charge and is, therefore, the more likely site of peroxo protonation. In model **7**, the

(23) Kurtz, D. M., Jr. *Essays Biochem.* **1999**, *34*, 85−100.

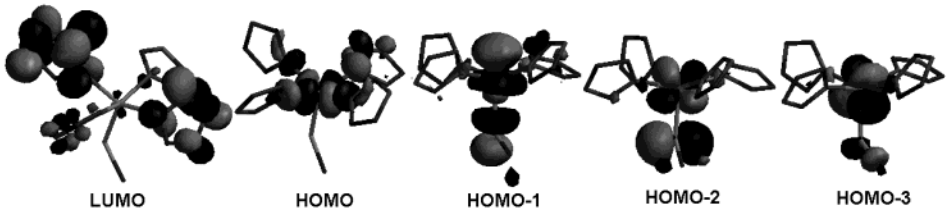

Figure 3. Frontier orbitals for the geometry-optimized high-spin ($S = 2$) ferrous model **1**. Shown are the β components of the four singly occupied orbitals (labeled HOMO and HOMO − 1, 2, 3), and of the lowest unoccupied orbital (labeled LUMO). The α (spin-up) and β (spin-down) orbitals were essentially identical in terms of spatial orientation. LUMO + 1, 2, 3, and so forth (not shown), which are closely spaced in energy, are localized on the various imidazoles in the same manner as LUMO.

Fe−O bond was significantly lengthened, and the Fe−S bond was significantly shortened compared to those of model **4** (cf. Table 2), also as expected for protonation of the coordinated oxygen.

A search of the Cambridge Structural Database[24] showed the average metal-peroxo bond length in end-on complexes to be 1.90 Å, with values in the range 1.84−2.00 Å. Our calculated Fe−O bonds are within this experimental range, with the most energetically favored models, $S = {}^1/_2$, **4**, and **6**, very close to the experimental average, which is suggestive of reasonable thermodynamic stability.

Because the ammonium group of a conserved lysine residue is present near the SOR iron site,[1,2] geometry optimizations were carried out on models **12**−**14** (cf. Figure 1), in which a $CH_3NH_3^+$ unit was placed within hydrogen bonding distance of either one oxygen atom of an end-on or side-on $[Fe-O_2]^+$ complex. $S = {}^5/_2$ as well as $S = {}^1/_2$ states were considered. The ammonium−peroxo distance was not constrained during optimization. In all cases, geometry optimization resulted in migration of the proton from the ammonium unit to the closest oxygen atom, yielding Fe−O−OH or Fe−O(H)−O complexes that were essentially identical to DFT-optimized models **6** and **7**, that is, in the absence of the methylammonium moiety. For the side-on peroxo model **14** ($S = {}^5/_2$), geometry optimization resulted in an end-on ferric-hydroperoxo unit identical to $S = {}^5/_2$ model **6**. However, DFT optimization of low-spin ($S = {}^1/_2$) model **15**, in which a water molecule rather than $CH_3NH_3^+$ was placed near the terminal oxygen, resulted in $O_{peroxo}\cdots O_{water}$ distance 2.72 Å consistent with hydrogen bond formation, rather than proton transfer from water.

Regardless of the coordination mode of the peroxo, results on models **12**−**14** support protonation by an alkylammonium unit (modeling the lysine side chain at the SOR active site), so that a low-spin, end-on ferric-hydroperoxo complex would be readily formed. Exact determinations of energy barriers for proton transfer in models **12**−**14** were not attempted, as such calculations would have to take into account protein and solvent effects, and, the dynamics of the highly mobile solvent-exposed polypeptide loop of the SORs, which contains the Lys48.[2]

$[FeO_2H_2]^{3+}$ and $[FeO]^{3+}$Complexes. Modeling of side-on (bidentate) ligation of formally Fe(III) to H_2O_2, that is, an $[FeO_2H_2]^{3+}$ complex (low-spin, model **11** in Figure 1), resulted in cleavage of the O−O bond. The computed HO$\cdots$OH distance was calculated to be >2.30 Å, with Fe−O distances at ∼1.90; furthermore, the Fe−His119 and Fe−His69 bonds were broken during geometry optimization. Such geometry would be impossible to attain within the native SOR active site, and this model **11** was, therefore, not considered further. For the end-on H_2O_2 complex, model **8** ($S = {}^5/_2$), geometry optimization proceeded with no minimum being found for the complex; rather, the optimized geometry resulted in a pentacoordinated Fe(III) site and free H_2O_2. Protonation of an Fe−O−OH complex (model **6** in Figure 1) at the terminal oxygen atom was also modeled. Geometry optimization for the high-spin ferric $[Fe-O-OH_2]^{3+}$ complex (model **9** in Figure 1) resulted in O−O bond dissociation, yielding water and an $[FeO]^{3+}$ complex. To confirm the feasibility of this modeled O−O bond cleavage, the geometry of the putative $[FeO]^{3+}$ complex (model **16** in Figure 1) was optimized, yielding bond lengths (cf. Table 2) similar to those obtained starting from model **11**.

Computed Electronic Absorption Spectrum. ZINDO-S/CI was employed in order to estimate the electronic absorption spectrum of the DFT-optimized $S = {}^1/_2$ end-on ferric-hydroperoxo model **6**, which, together with $S = {}^1/_2$ model **4**, is the most likely candidate of the models tested for the experimentally observed 600-nm intermediate.[25] The ferric SOR sites with carboxylate or hydroxide as the sixth ligand are known to have strong LMCT absorption bands at ∼650 and 600, respectively.[5−7] On the basis of resonance Raman results as well as comparison with better-characterized Fe−S complexes, a CysS → Fe(III) with some His → Fe(III) CT character was assigned to these bands.[6,7] The calculated electronic absorption spectrum for the $S = {}^1/_2$ end-on ferric-hydroperoxo model, **4**, features one single prominent band in the visible region, which, as illustrated in Figure 4, has a mostly H_3C-S → Fe(III) π CT character with some imidazole → Fe(III) but very little peroxo → Fe(III) CT character. The calculated wavelength of this band, 440 nm, does not match the experimental value of 600 nm, a problem previously encountered with this computational methodology, which is often treated by adjustments of structural parameters to give better agreement between calculated and observed spectra.[26] We did indeed find that only minor geometrical changes (i.e., Fe−S or Fe−O bond lengths, N−Fe−O−O

(24) Allen, F. H.; Kennard, O. *Chem. Des. Autom. News* **1993**, *1*, 31−37.

(25) Similar ZINDO/S-CI calculations were performed on $S = {}^1/_2$ model **4** (low-spin end-on peroxo). Because results on models **4** and **6** were essentially identical (i.e., they both feature one single strong transition in the visible domain, arising from sulfur-to-iron charge transfer with some imidazole-to-iron contribution), only results on $S = {}^1/_2$ model **6** are reported here.

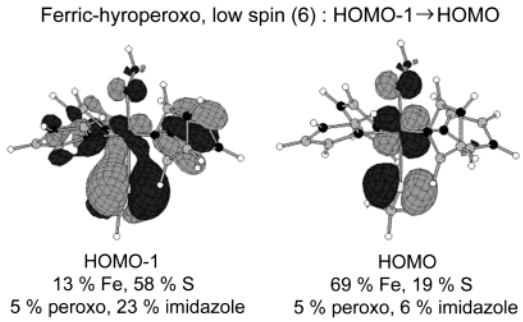

Figure 4. The main orbitals responsible for the low-energy (440 nm, oscillator strength 0.024) ligand-to-Fe(III) CT band in the ZINDO-S/CI-calculated electronic absorption spectra of the $S = {}^1/_2$ end-on ferric-peroxo SOR model **4**. Percentage contributions listed below each orbital were calculated by summing the squares of the coefficients of the respective atomic orbitals.

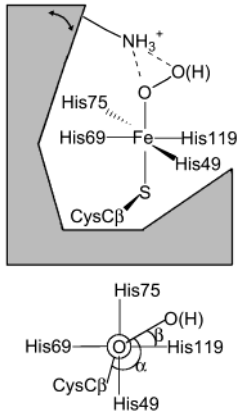

Figure 5. Schematic diagram of the ferric-(hydro)peroxo intermediate in SOR based on models **4** and **6**. Top: the protein matrix is indicated in gray, and the double arrow indicates movement of the polypeptide loop containing Lys48. Glu47 is not shown because kinetic evidence indicates that it is not involved in the rate-limiting step of peroxide release at basic pH.[9] Bottom: view along the O−Fe−S axis. Allowed values of dihedral angles α and β are listed in Table 2.

dihedrals, or the orientation of the histidine planes) brought about significant shifts in the energy and oscillator strength of the 440-nm calculated transition. For example, changing the N−Fe−O−O dihedral angle (β in Figure 5) in model **4** from 45° to 14° caused the 440-nm band to shift to 520 nm.

Discussion

The Ferrous Pentacoordinated and Ferric-Carboxylate Models. A previous DFT (B3LYP) study[27] on the ferrous SOR site (model **1** in Figure 1) assumed an $S = 2$ state and calculated an Fe−S bond length of 2.34 Å and Fe−N bond lengths of 2.18, 2.18, 2.29, and 2.30 Å (with no geometrical constraints imposed).[28] The authors of the B3LYP study ascribed the differences in bond lengths between the four Fe−N bonds to CH•• •S(Cys) hydrogen bonding between the iron-ligated sulfur and two of the imidazole ligands. Our results obtained on the same model (**1**) with no geometrical constraints imposed (data not shown) confirmed that imidazoles 69 and 119 have a tendency to form C−H hydrogen bonds to the thiolate ligand. However, these hydrogen bonds do not form in the constrained model, nor is there any indication of such interactions in SORs.[1,2,29] Instead, in the SORs, a peptide NH, which lies below the His119 imidazole ring, is a hydrogen bond donor to the cysteine sulfur ligand. A more distant backbone NH group of Leu117 may form a second, weaker N−H···S hydrogen bond. The steric constraints imposed by the protein matrix on the imidazole ring orientations already discussed also make these unconstrained models unrealistic.

X-ray diffraction,[1] EXAFS, and MCD[7] all indicated that the ferrous SOR site is pentacoordinated. The question arises as to why this solvent-exposed site bearing an overall +1 charge should remain pentacoordinated. Our DFT results on ferrous water-ligated model **2** indicate that the interaction between the ferrous pentacoordinated SOR model and a water molecule is very weak. Examination of the LUMOs of the high-spin ferrous pentacoordinated model **1** (Figure 3) reveals the absence of low-lying iron-localized unoccupied orbitals with substantial d character, which would limit efficient interaction of nucleophilic ligands with the iron except for free radical ligands, which can take advantage of the partially occupied iron d orbitals. The positively charged SOR site would also be expected to interact more strongly with a negatively charged than a neutral sixth ligand. Superoxide is both a radical and negatively charged at neutral pH (HO_2 $pK_a \sim 4.7$), and therefore, appears to be particularly well-suited to interact with the pentacoordinated SOR site. On the other hand, the glutamate ligand serving as the sixth ligand in the resting ferric state of SORs is seen to dissociate from the active site upon reduction. On the basis of the results obtained on model **2**, one might have expected this glutamate to remain coordinated to iron in the ferrous form. However, this glutamate is located on a solvent-exposed, highly mobile, hydrophilic loop; the solvation energy of this loop and of the negatively charged carboxylate may account for the fact that the glutamate is not coordinated to the ferrous SOR site.

Superoxide has the potential of coordinating to iron in either a bent, end-on monodentate configuration (σ-interacting with the Fe d_{z^2} orbital and π-interacting with the Fe d_{xz}/d_{yz} orbitals) or a side-on bidentate configuration, interacting with Fe d_{xz}/d_{yz} orbitals (cf. Scheme 4). This interaction may, in theory, occur either between a partially filled d orbital on iron and the superoxide singly occupied HOMO (π^*), or between an empty iron d orbital (in low-spin complexes) and a filled superoxide π^* HOMO − 1 orbital. The former case would favor reductive binding of the superoxide, yielding a diamagnetic peroxo ligand, while the latter case would favor retention of superoxo and ferrous characters.

(26) Neese, F.; Zaleski, M.; Loeb, K.; Solomon, E. I. *J. Am. Chem. Soc.* **2000**, *122*, 11703−11724.
(27) Sigfridsson, E.; Olsson, M. H. M.; Ryde, U. *Inorg. Chem.* **2001**, *40*, 2509−2519.
(28) The B3LYP study by Sigfridsson et al. yields an Fe−S bond length (2.34 Å) that is in good agreement with the 2.37-Å distance determined by EXAFS of *P. furiosus* SOR. The difference between the B3LYP results and our data (Fe−S 2.25 Å) is likely due to the hybrid (Hartree−Fock/DFT) character of the B3LYP functional. A Hartree−Fock/3-21G* geometry optimization on our model **1** (our unpublished results) yielded a longer Fe−S bond, 2.47 Å.
(29) Indeed, there is no indication of C−H···S hydrogen bonds between histidines and cysteines in any protein. See: Baures, P. W.; Beatty, A. M.; Dhanasekaran, M.; Helfrich, B. A.; Perez-Segarra, W.; Desper, J. *J. Am. Chem. Soc.* **2002**, *124*, 11315−11323.

Scheme 4

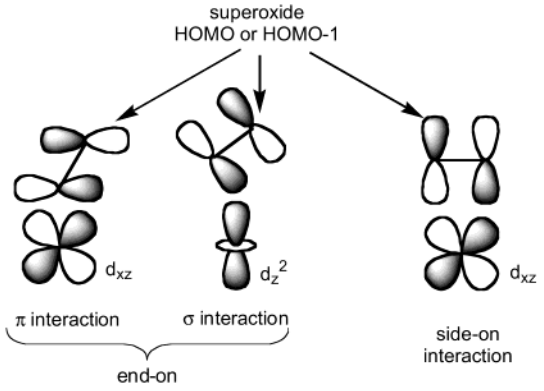

As shown in Figure 3 for high-spin ferrous model **1**, no LUMOs are localized on iron; however, HOMO − 1 has the appropriate shape and orientation for end-on binding, while HOMO − 2 is appropriate both for end-on π interaction as well as for side-on binding. The ferrous SOR site thus clearly favors reductive binding of superoxide via interaction with HOMO − 1 and HOMO − 2.

The geometrical parameters obtained in this work for the ferric acetate complex, **3**, as a model for the glutamate-bound ferric resting SOR site are in good agreement with those from the SOR crystal structures[1] and EXAFS[7] measurements. As observed experimentally,[5,7] ferric-acetate model **3** is predicted to be high-spin. EPR spectra of ferric SORs have been interpreted in terms of the coordination sphere being elongated along one N−Fe−N axis.[7] However, no evidence for an elongated (or compressed) N−Fe−N axis is found in the available crystal structures, and our DFT-optimized structure showed no evidence for such a distortion.

The 600-nm Intermediate in the Reaction of the Ferrous SOR Site with O_2^-. In agreement with previous formulations of the SOR catalytic cycle (cf. Scheme 1), our DFT results show that end-on peroxo and hydroperoxo models of the ferric SOR site are stable, with the low-spin states being energetically favored. While the putative intermediate described by models **4** and **6** has been previously proposed to be a ferrous-superoxo species,[11] the geometrical parameters, partial charges, and electronic absorption spectra computed in this work are all more consistent with a ferric-(hydro)peroxo formulation. The DFT-optimized $S = {}^1/_2$ and ${}^5/_2$ side-on ferric-peroxo models **5** featured severe elongation or dissociation of iron-imidazole bonds, which are unlikely at the SOR active site because of constraints imposed by the protein matrix,[20] and $S = {}^3/_2$ model **5** converts to an end-on geometry upon optimization. While characterized non-heme ferric-peroxo complexes are known to be $S = {}^5/_2$ and side-on coordinated,[30,31] the higher energies and unreasonable geometries of $S = {}^1/_2$ and ${}^5/_2$ models **5** are apparently due to steric interactions between the peroxo ligand and the constrained imidazole rings (cf. Figure 2). On the other hand, our prediction that the ferric-hydroperoxo SOR complex would be end-on, $S = {}^1/_2$, is consistent with previously reported non-heme ferric-hydroperoxo and -alkylperoxo complexes.[30,31]

Recently, reaction of superoxide with an $S = 2$ ferrous SOR model complex in methanol afforded a metastable complex formulated as low-spin, end-on ferric-hydroperoxo.[32] All non-heme-iron ferric-peroxo complexes reported to date are observable only at high pH values or in aprotic solvents. Upon exposure of these ferric-peroxo complexes to a source of protons, the corresponding hydroperoxo complexes are immediately detected.[30,31] These experimental observations favor a ferric-hydroperoxo over ferric-peroxo for the 600-nm intermediate. Our calculations, however, do not address the rates of these proton transfers. It is important to note that no solvent deuterium isotope effect was observed on the rate of formation of the 600-nm intermediate, implying that protonation of the ferric-peroxo would have to exceed what is apparently a diffusion-controlled rate of formation of the 600-nm intermediate.[9]

The experimentally observed 600-nm band of the transient intermediate in the SOR catalytic cycle is predicted by our ZINDO/S-CI results to be due mainly to a CysS → Fe(III) π CT transition, with some HisN → Fe(III) π CT character ($S = {}^1/_2$ ferric-hydroperoxo model, cf. Figure 4). This band had been tentatively assigned to some combination of peroxo → Fe(III) and CysS → Fe(III) π CT characters.[8] Electronic absorption spectra of many non-heme iron (hydro)peroxo complexes are dominated in the visible region by a peroxo → Fe(III) π CT absorption near 600 nm.[31] An exception is the hydroperoxo adduct of ferric bleomycin, which, on the basis of analysis of its MCD and absorption spectra, shows no evidence of a strong peroxo → Fe(III) π CT transition in the visible region. The optical absorption spectrum is instead dominated by a N → Fe(III) π CT transition (∼380 nm) originating from a deprotonated amide ligand.[31] The presence of the strongly π-interacting deprotonated amide differentiates the bleomycin hydroperoxo adduct from other known non-heme iron (hydro)peroxo complexes. Our results suggest that complexes containing a strongly π-interacting anionic ligand (a deprotonated amide in bleomycin, or a thiolate in SORs) would not exhibit significant peroxo → Fe(III) π CT transitions in the visible region of the spectrum. Apparently, the anionic π-interacting ligand can be either trans (as in SORs) or cis (as in bleomycin) to the peroxide.

It has been suggested that the Cβ−S−Fe−O−O unit of the putative (hydro)peroxo intermediate of SOR would be planar in order to maximize π overlap.[22] However, maximal ferric-peroxo bonding interactions within this intermediate would not necessarily be optimal for rapid enzymatic *turnover* of superoxide to hydrogen peroxide. In fact, the Cβ−S−Fe−O−O unit is decidedly nonplanar in our models; the range of the Cβ−S···O−O dihedral angle α in Figure 5, is 64−150° (cf. Table 3). Dihedral angles outside this range appear to be prevented by steric contacts between the peroxo

(30) Girerd, J.; Banse, F.; Simaan, A. *Struct. Bonding (Berlin)* **2000**, *97*, 145−176.
(31) Solomon, E. I.; Brunold, T. C.; Davis, M. I.; Kemsley, J. N.; Lee, S. K.; Lehnert, N.; Neese, N.; Skulan, A. J.; Yang, Y. S.; Zhou, Z. *Chem. Rev.* **2000**, *100*, 235−350.
(32) Shearer, J.; Scarrow, R. C.; Kovacs, J. A. *J. Am. Chem. Soc.* **2002**, *124*, 11707−11717.

oxygens and imidazole rings. It is noteworthy that these constraints on the O−O orientation correspond to the most solvent-accessible direction of approach to the SOR iron site. Despite the nonplanarity, the frontier orbitals of the S−Fe−O−O unit in the terminally coordinated peroxo models (as exemplified for model **6** in Figure 4) exhibit π character, with the HOMOs being predominantly π antibonding in character.

Implications for the SOR Mechanism. Three possible pathways were illustrated in Scheme 3 for breakdown of the ferric-peroxo species formed upon diffusion-controlled reaction of the "resting" ferrous SOR site with superoxide: (1) The ferric-peroxo is protonated on the iron-coordinated oxygen atom by the proximal lysine residue, to yield a $[Fe-O(H)-O]^{2+}$ complex with a considerably weakened Fe−O bond, leading to dissociation of OOH^-. This dissociation may or may not out-compete a second protonation, to yield a $[Fe-O(H)-OH]^{3+}$ "complex", which our modeling results show is not stable and dissociates to yield H_2O_2 and a pentacoordinated ferric SOR site. (2) The ferric-peroxo is protonated on the terminal (non iron-coordinated) oxygen atom to yield a [Fe−O−OH] unit. The hydroperoxo could be displaced by another ligand (the carboxylate group of Glu47), or by protonation of the coordinated oxygen to yield the unstable $[Fe-O(H)-OH]^{3+}$ species. (3) The terminal oxygen of the ferric-peroxo is doubly protonated, to yield a $[Fe-O-OH_2]^{3+}$ species, which then spontaneously dissociates to yield water and a $[FeO]^{3+}$ ferryl complex.

A fourth hypothetical pathway would involve outer-sphere oxidation of the ferrous SOR site by superoxide, to yield a ferric pentacoordinated transient species that would then decay to the "resting" ferric carboxylate-bound state. However, kinetic measurements using outer-sphere oxidants such as ferricyanide do not yield a 600-nm absorbing intermediate with SOR.[9]

With the caveat that our DFT results do not address kinetics, pathway 2 is favored over pathway 1 by the distribution of the partial charges within the iron-coordinated peroxo moiety in model **4** (cf. Table 3). The terminal oxygen atom bears a more negative charge than does the iron-bound oxygen, and on this basis, the terminal oxygen atom should be the preferred site of protonation. Furthermore, the DFT results indicate models **7**, with the coordinated oxygen protonated, to be significantly less stable than the terminally protonated models **6**. Although nucleophilic displacement of the peroxo ligand by the conserved carboxylate of Glu47 is an attractive mechanism, removal of the conserved carboxylate side-chain by site-directed mutagenesis had no effect on the 50 s^{-1} decay of the 600-nm intermediate at basic pHs.[8,9] Thus, to leave the active site via pathway 2, the peroxo ligand would either have to be twice protonated, or the Fe−O bond in the $S = {}^1/_2$ ferric-hydroperoxo complex would have to cleave spontaneously. Spontaneous (unassisted) cleavage of the Fe−O bond in [Fe−O−OH] seems much less likely, in view of the reasonably short Fe−O bond in the low-spin, ferric-hydroperoxo model **4**. The oxygen atoms of the peroxo ligand may be protonated either by the conserved Lys48 or, at acidic pHs, by the protonated Glu47

Scheme 5

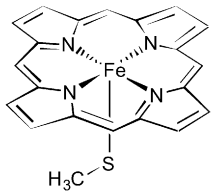

carboxylate or by H_3O^+.[9] Figure 5 schematically depicts the orientation of Lys48 and the ligands of the putative ferric (hydro)peroxo intermediate on the basis of our modeling results and steric restrictions imposed by the protein. Comparisons of the geometrical parameters of models **4** and **6** (cf. Table 2) indicate that protonation of the terminal oxygen of the peroxo ligand results in significant shortening of the Fe−S bond (by ∼0.15 Å for low-spin models **4** and **6**), but no lengthening of the Fe−O(peroxo) bond. Changes in Fe−S bond lengths on the order of 0.2 Å are likely to be allowed by the protein matrix, as suggested by the conservative range of 2.3−2.5 Å for the Fe−S bonds in the available SOR crystal structures.[1,2] It has been argued that one role of the thiolate ligand in SORs[7] could be to "push" electron density onto the iron, thereby promoting ferrous-to-superoxide electron transfer and/or facilitating H_2O_2 dissociation. Regarding the latter, our results indicate that hydrogen peroxide release is dependent on double protonation of the peroxo ligand.

Comparison with Cytochrome P450. The structure of the SOR site resembles that of the heme-thiolate unit encountered in the active site of cytochromes P450 (cf. Scheme 5).[33] In both cases, the iron is coordinated by four aza atoms in the equatorial plane while a cysteinate serves as the axial ligand. Despite the apparent structural similarity, the functions of SORs and cytochromes P450 differ significantly. P450s function as mono-oxygenases, while there is no report of SORs possessing oxygenase activity. In fact, the ferrous SOR site is air-stable and decidedly unreactive with molecular oxygen. The active oxygenating species in P450 is proposed to be a ferryl $[FeO]^{3+}$ resulting from O−O bond cleavage in a preceding ferric-peroxo species (although other mechanisms may apply under particular conditions).[33]

DFT[34] and subsequent QM/MM studies,[35,36] on heme-thiolate, end-on $[FeO_2]^+$ models of cytochrome P450 led to the suggestion that double protonation of the terminal oxygen is essential for O−O bond cleavage to create the active ferryl species and to avoid hydrogen peroxide release. The active site is buried in cytochrome P450,[33] and protons are proposed to be selectively delivered to the $[FeO_2]^+$ complex by a network of hydrogen-bonded water molecules. Our DFT results show that pathway 3 in Scheme 3, that is, O−O bond cleavage from a formally ferric-peroxo $[Fe-O_2H_2]^{3+}$ species to form a ferryl $[FeO]^{3+}$ species, may also be feasible for SOR. Unlike cytochrome P450, however, the SOR active

(33) Sono, M.; Roach, M. P.; Coulter, E. D.; Dawson, J. H. *Chem. Rev.* **1996**, *96*, 2841−2887.
(34) Harris, D. L.; Loew, G. H. *J. Am. Chem. Soc.* **1998**, *120*, 8941−8948.
(35) Harris, D. L. *J. Inorg. Biochem.* **2002**, *91*, 568−585.
(36) Ogliaro, F.; de Visser, S. P.; Cohen, S.; Sharma, P. K.; Shaik, S. *J. Am. Chem. Soc.* **2002**, *124*, 2806−2817.

site is solvent-exposed, presumably giving it much greater access to protons.[1,2] Furthermore, the charge distribution in our ferric-hydroperoxo model **6** indicates the iron-bound oxygen atom to be a better proton acceptor than the already protonated terminal oxygen atom of the same complex. Thus, unrestricted solvent exposure of a ferric-hydroperoxo SOR site would seem to favor protonation of the iron-bound oxygen and, thereby, hydrogen peroxide release over O−O bond cleavage. The presence of the ammonium group of the conserved Lys48 near the peroxo ligand may also contribute to selective protonation of the iron-coordinated oxygen atom in model **6**. Accordingly, no published experimental evidence supports pathway 3 of Scheme 3 in SORs.

Conclusions and Summary. DFT and ZINDO/S-CI results support previous assignments of the SOR 600-nm intermediate observed during reduction of superoxide as a ferric-(hydro)peroxo complex and favor a low-spin, end-on (hydro)peroxo description. Constraints on the imidazole ligand ring orientations imposed by the protein matrix favor the end-on over side-on peroxo coordination geometry and a decidedly nonplanar CysCβS−Fe−O−O unit. The absorption band of this intermediate is shown to be due mainly to a CysS $\rightarrow$ Fe(III) π LMCT transition, and to involve imidazole-localized orbitals to a lesser extent.

Acknowledgment. We thank Joseph Emerson, Dr. M. K. Johnson, and M. Clay (UGA Chemistry Department) as well as Drs. H.F. Schaefer, W. Allen, and C. Barden (UGA Center for Computational Quantum Chemistry) for helpful discussions.

Note Added in Proof: A recently reported ferric-peroxo species resulting from reaction of E47A SOR with H_2O_2 was suggested to have a side-on peroxo bonding geometry (Mathé, C.; Mattioli, T. A.; Horner, O.; Lombard, M.; Latour, J.-M.; Fontecave, M.; Nivière, V. *J. Am. Chem. Soc.* **2002**, *124*, 4966−4967). If so, our calculations indicate that this species is unlikely to be an intermediate in the reduction of superoxide catalyzed by SOR.

Supporting Information Available: Listing of DFT-optimized atomic coordinates, energies, and spin populations of models discussed throughout the paper. This material is available free of charge via the Internet at http://pubs.acs.org.

IC025684L